CrossMark

Excitation Temperature and Constituent Concentration Profiles of the Plasma Jet Under Plasma Spray-PVD Conditions

Wenting He[1] · Georg Mauer[1] · Robert Vaßen[1]

Abstract Plasma spray-physical vapor deposition (PS-PVD) is a promising technology to produce columnar structured thermal barrier coatings with excellent cyclic lifetime. The characteristics of plasma jets generated by standard plasma gases in the PS-PVD process, argon and helium, have been studied by optical emission spectroscopy. Abel inversion was introduced to reconstruct the spatial characteristics. In the central area of the plasma jet, the ionization of argon was found to be one of the reasons for low emission of atomic argon. Another reason could be the demixing so that helium prevails around the central axis of the plasma jet. The excitation temperature of argon was calculated by the Boltzmann plot method. Its values decreased from the center to the edge of the plasma jet. Applying the same method, a spurious high excitation temperature of helium was obtained, which could be caused by the strong deviation from local thermal equilibrium of helium. The addition of hydrogen into plasma gases leads to a lower excitation temperature, however a higher substrate temperature due to the high thermal conductivity induced by the dissociation of hydrogen. A loading effect is exerted by the feedstock powder on the plasma jet, which was found to reduce the average excitation temperature considerably by more than 700 K in the Ar/He jet.

Keywords Plasma spray-PVD · Ar/He plasma jet · Excitation temperature · Powder loading effect

Introduction

Plasma Spray-Physical Vapor Deposition (PS-PVD) is a novel technology, which has been developed with the aim of depositing uniform and thin coatings with large area coverage [1]. Compared with conventional atmospheric plasma spraying (APS), the very low working chamber pressure of 50 to 200 Pa leads to an expansion of the plasma jet so that

---

✉ Wenting He
  w.he@fz-juelich.de

1   Forschungszentrum Jülich GmbH, IEK-1, Jülich, Germany

the plasma jet experiences unconventional properties, showing higher velocities and low densities compared with the APS jets [2]. With an increasing input power of the plasma torch up to 180 kW, the plasma jet is expected to have high temperatures, exceeding the limitations of the conventional plasma temperature diagnostic method such as enthalpy probe [3]. Moreover, in PS-PVD, the major fraction of the injected feedstock powder is transformed into vapor phase. As a consequence, the diagnostics based on the thermal emission of solid or liquid particles, for example by the DPV-2000, are not applicable. Optical emission spectroscopy (OES) however can be used to determine the properties of the plasma jet [4–8] and was also introduced to characterize the injected material in thermal spray processes such as the VPS/LPPS [9].

In the PS-PVD process, the plasma gases can be different, such as argon, helium, hydrogen, nitrogen [10] or mixtures of them. The composition of the plasma gas has a significant influence on the microstructures of the PS-PVD coatings [11–15]. A standard plasma gas mixture of argon and helium is normally used to manufacture columnar structured ceramic coatings which have shown excellent performance in cyclic lifetime tests [16]. In earlier studies, the typical plasma characteristics of the PS-PVD process and the impact on the coating properties were investigated by OES [14, 17]. However, the calculation of the excitation temperature was based on the integral intensity through the line of measurement of OES and the assumption of (partial) local thermal equilibrium (LTE or pLTE). Due to the expansion of the plasma jet at low chamber pressure, the concentrations of all species are reduced, also the one of the electrons. Therefore, the LTE conditions are not satisfied especially due to the fast diffusion of electrons at the plasma fringes. So the influence of the deviation from LTE and its effect on the calculation of excitation temperature should be taken into consideration in order to obtain a more accurate description of the plasma jet.

Moreover, the addition of H_2 as a secondary plasma gas results in a broadened plasma jet [18] as well as in more compact columnar coating microstructures [15]. The microstructures and preferred growth orientations of columnar structured coatings were shown to be related to the substrate temperature [19]. In this paper, two different PS-PVD jets composed by Ar/He and Ar/He/H_2 were investigated. Abel inversion was introduced to reconstruct the spatial characteristics of the plasma jet including the excitation temperatures along the radial direction and the distribution of atomic Ar and He in the Ar/He jet. The deviation from LTE on the calculation of excitation temperatures by different emission lines of Ar and He is discussed. Besides, the influences of the addition of H_2 as plasma gas on the excitation temperature profile and substrate temperature were analyzed. Furthermore, the effect of feedstock powder loading was investigated with respect to the reduction of the temperature of the plasma jet.

Experimental Methods and Evaluation Principles

Plasma characteristics were determined by OES, which is widely used in non-transferred plasma arc systems [20] to detect the emitting gas species [3]. Based on the measured emission spectra, the excitation temperatures in the plasma can be determined by the Boltzmann plot method [14]. However, as the plasma jet is optically thin, the lateral setup of OES allows collecting only the integral intensities of the spectral lines along the line of measurement. In order to obtain the localized emission profile through the radial direction of the plasma jet, Abel inversion has to be performed to transform the measured intensity into radial emission if the plasma is cylindrically symmetric [21].

Experimental Setup

The plasma jets were generated by an O3CP torch in an Oerlikon (formerly Sulzer) Metco Multicoat system, which can achieve a low working pressure of 200 Pa in the chamber and a net power of 60 kW. The input plasma gases and other spray parameters are given in Table 1. Two different plasma jets were generated with different input constituents of plasma gases: (A) Ar and He and (B) Ar, He, and H_2. In both plasma jets, the net power was maintained at 60 kW. During spraying, four standard liters per minute (slpm) of oxygen was led into the chamber to keep the parameters consistent with the real coating process. The measurement position was located at a spraying distance (axial distance away from the torch) of 1000 mm. The feedstock powder was an agglomeration of monoclinic ZrO_2 and 7 wt% cubic Y_2O_3 primary particles produced by Oerlikon Metco designated as M6700. The substrate temperatures were monitored by a CHINO IR-AP 3CG pyrometer, which is a monochromatic narrow wavelength band radiation thermometer measuring the temperature range of 500 to 1500 °C at a wavelength of 1.6 μm. It should be noted that in OES measurements, there were no samples in the plasma jet.

The spectrometer was an ARYELLE 200 manufactured by Laser Technik Berlin (LTB), Berlin, Germany. Plasma radiation was collected through a borosilicate glass window and an achromatic lens, transferred by an optical fiber to the 50 μm entrance slit of the spectrometer and detected by a 1024 × 1024 pixels CCD array. The system is equipped with an Echelle grating, and the spectral resolution obtained is 15.9–31.8 pm [14]. The scanning wavelength range is 381–786 nm, which was calibrated by a standard Hg lamp. Besides, the exposure time for the OES measurement was 400 ms. According to Ref. [22], the fluctuations frequency of the voltage spectra peaks are in the range of 4–11 kHz. In other words, it is in a time scale of 0.25–0.1 ms. Thus, the fluctuations in the plasma jet should not affect the measured intensities.

Evaluation Principles

Boltzmann Plot

The Boltzmann plot method is valid for LTE or pLTE conditions [3]. By applying the Boltzmann distribution, the absolute intensity I_{jk} of a spectral line emitted by the plasma due to the transition from an excited state j to a low an energy state k is

Table 1 Plasma parameters for diagnostics

Conditions	A-200	A-1000	B-200
Plasma gases	Ar 35 slpm/He 60 slpm		Ar 35 slpm/He 60 slpm/H_2 10 slpm
Current	2750 A		2200 A
Net power	60 kW		
Carrier gas	2 × 16 slpm		
Chamber pressures	200 Pa	1000 Pa	200 Pa
Spray distance	1000 mm		
Powder feed rate	0∼18 g/min		6.9 g/min

$$I_{jk} = \frac{Lhc}{4\pi\lambda_{jk}} A_{jk} n \frac{g_j}{z} e^{\left(\frac{-E_j}{k_B T exc}\right)} \tag{1}$$

wherein, L is the emission source depth, h is the Planck constant, c is the velocity of light, A_{jk} is the transition probability, n is the density of emitting atoms/ions, g_j is the statistical weight of the excited level j, λ_{jk} is the wavelength of the emission, Z is the partition function, E_j is the energy of the excited level, k_B is the Boltzmann constant, and T_{exc} is the excitation temperature. If a series of emission lines of transitions to a lower energy level k are measured, a linear plot is obtained with $ln\left(\frac{I_{jk}\lambda_{jk}}{g_j A_{jk}}\right)$ as a linear function of E_j as shown by Eq. (2). The excitation temperature T_{exc} is yielded from the slope.

$$ln\left(\frac{I_{jk}\lambda_{jk}}{g_j A_{jk}}\right) = \frac{-1}{k_B T_{exc}} E_j + C, C = ln\left(\frac{Lhcn}{4\pi Z}\right) \tag{2}$$

The left side of this equation is the so-called atomic-state distribution function (ASDF). Wherein, λ_{jk}, A_{jk}, g_j and E_j can be retrieved e.g. from NIST Atomic Spectra Database [23]. I_{jk} were directly taken from the peak value of the emission lines in the measured spectra.

However, laboratory plasma jets are seldom in LTE. According to Ref. [24], two situations of departure from LTE can be observed considering the density of the low energy levels relative to the density that they would have if they were in equilibrium with the high energy levels. Depending on the conditions, the lower energy levels are over-populated (in a so-called ionizing plasma) or underpopulated (in a recombining plasma) with respect to the Saha–Boltzmann population distribution [25]. Under PS-PVD conditions, where the expanding plasma jet in a chamber is at a pressure of few tens of Pascals, deviations from LTE occur because the electron density (n_e) decreases (the rate of electron energy loss per unit volume is proportional to n_e) [26]. Due to the reduction of energy exchange by collisions, the electron temperature T_e can be higher than that of heavy species T_h [27]. Only the higher energy levels can be in pLTE and therefore represent the correct excitation temperature [28]. Besides, it was found that helium plasmas exhibit strong deviations even in those situations where a comparable argon plasma is close to equilibrium [29], thus neutral argon (Ar I) lines are used to calculate the excitation temperature in the Ar/He jet as well as in the Ar/He/H$_2$ jet.

All of the intensities of the emission lines were measured by OES at a spraying distance of 1000 mm. In the example of a Boltzmann plot (Fig. 1), fifteen Ar I lines are plotted (the spectroscopic data for the 15 Ar lines are listed in Table 2), but four points of low energy level transitions (4p–4s) were discarded because they are not aligned linearly with the other 11 higher energy level transitions (4d, 5d, 6s, 6d–4p). The reason is the deviation from LTE as mentioned above. The measured intensities of the 11 Ar I emission lines have mean absolute percentage deviations of $4\sim8\%$ in the radius range of 130 mm.

Abel Inversion

Assuming the plasma jet to be cylindrically symmetric, as shown in Fig. 2, the laterally measured intensity $I(y)$ at the measurement distance y_k contains the local emission intensity $\varepsilon(r)$ of all the plasma radial positions along the line of measurement (from $-x_0$ to x_0), given as Eq. (3):
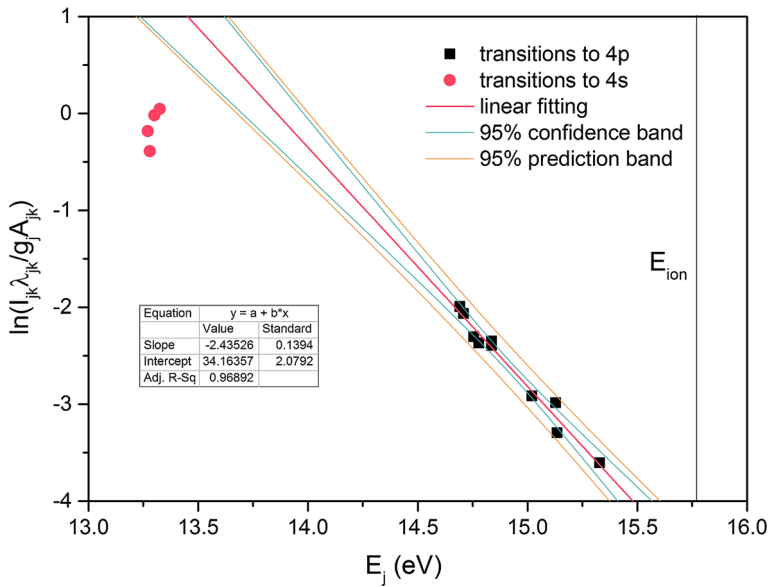
Fig. 1 Example of a Boltzmann plot for 15 Ar I emission lines under condition A-200 (Ar/He jet, 200 Pa)

Table 2 Ar I lines used in determining the excitation temperature through Boltzmann plot

λ (nm)	I_{jk} (a.u.)	A_{jk} (s^{-1})	g_j	$\ln(I\lambda/gA)$	E_k (eV)	Trans.
549.5874	743.6	1.69E+06	9	−3.61679	15.32	6d–4p
555.8702	483.5	1.42E+06	5	−3.27402	15.13	5d–4p
603.2127	1879.6	2.46E+06	9	−2.97181	15.13	5d–4p
641.6307	817.7	1.16E+06	5	−2.40286	14.84	6s–4p
687.1289	1541.2	2.78E+06	3	−2.06374	14.71	4d–4p
693.7664	602.2	3.08E+06	1	−1.99772	14.69	4d–4p
703.0251	1780.6	2.67E+06	5	−2.36693	14.84	6s–4p
720.6980	562.5	2.48E+06	3	−2.90977	15.02	6s–4p
735.3293	847.2	9.60E+05	7	−2.37834	14.78	4d–4p
737.2118	2342.2	1.90E+06	9	−2.29287	14.75	4d–4p
743.5368	574.1	9.00E+05	5	−2.35537	14.84	6s–4p
696.5431	28,791.1	6.39E+06	3	0.04509	13.33	4p–4s
714.7042	1777	6.25E+05	3	−0.38957	13.28	4p–4s
738.398	56,332	8.47E+06	5	−0.01798	13.30	4p–4s
751.4652	44,592.5	4.02E+07	1	−0.18203	13.27	4p–4s

$$I(y) = \int_{-x_0}^{x_0} \varepsilon(r)dx = 2\int_{0}^{x_0} \varepsilon(r)dx \qquad (3)$$

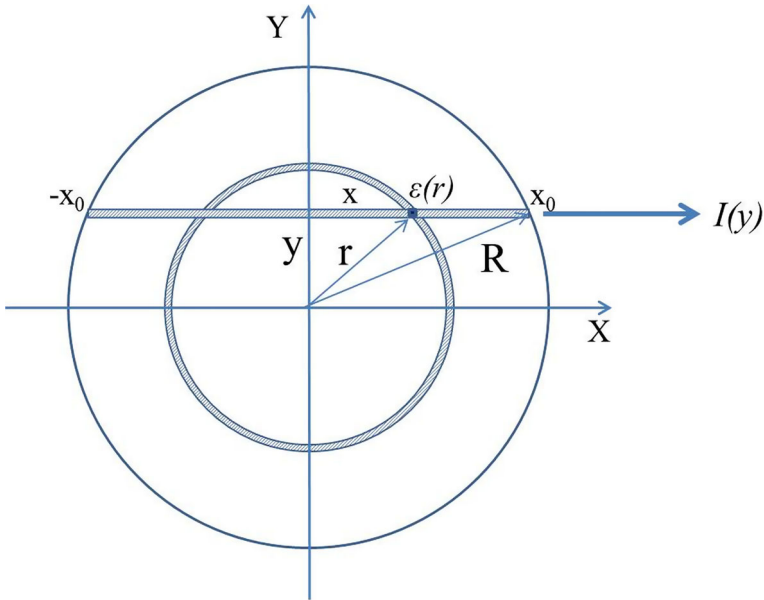The substitution $x = \sqrt{r^2 - y^2}$ is then introduced into Eq. (3) yielding the integral Eq. (4):

Fig. 2 Schematic illustration of Abel inversion in a plane perpendicular to the axis of the plasma jet

$$I(y) = 2 \int\limits_{y}^{R} \frac{\varepsilon(r)}{\sqrt{r^2 - y^2}} r dr \qquad (4)$$

The calculated temperature depending on $I(y)$ is therefore called the average excitation temperature $T_{exc}^{(A)}$. In order to know the local excitation temperature $T_{exc}(r)$, an Abel inversion [30] has to be used to reconstruct the radial $\varepsilon(r)$ from the measured $I(y)$ in Eq. (4) by Eq. (5):

$$\varepsilon(r) = -\frac{1}{\pi} \int\limits_{r}^{R} \frac{\frac{dI(y)}{dy}}{\sqrt{y^2 - r^2}} dy \qquad (5)$$

The photos of the plasma jets and the measured intensity distributions through the whole plasma jets under different conditions were published in Ref. [18]. They show that the intensity distributions are axisymmetric indicating the reliability of the Abel inversion. Therefore, in this paper, only half of the intensity distributions are presented.

As the Abel inversion amplifies the noise in the raw data as well as requires the intensity to fall to zero at the plasma edge, it is better to reduce the noise before data processing. It was found that polynomial fitting can be used to partially filter out noise in the raw data [31]. Therefore, before Abel inversion, the laterally measured intensity profiles were fitted by polynomials.

Because the measured $I(y)$ is not given analytically but in discrete data points, both the differentiation and the integration in Eq. (5) cannot be performed directly. There are many different methods to perform Abel inversion to reconstruct a density distribution from a measured line-integral. G. Pretzler et al. proposed the Fourier method [32] to perform the

calculation in one single step. Comparing different reconstruction techniques by the methods of error propagation, the Fourier method shows the best results because it also works as a low-pass filter [33].

In the Fourier method, the unknown distribution $\varepsilon(r)$ is expanded in a series similar to a Fourier-series:

$$\varepsilon(r) = \sum_{n=N_l}^{N_u} A_n \varepsilon_n(r) \tag{6}$$

with unknown amplitudes A_n, where $\varepsilon_n(r)$ is a set of cosine-functions, e.g.

$$\varepsilon_0(r) = 1, \varepsilon_n(r) = 1 - (-1)^n cos\left(n\pi \frac{r}{R}\right)(n \geq 1) \tag{7}$$

Following Eq. (4), the Abel transform of Eq. (6) has the form:

$$i(y) = 2\sum_{n=N_l}^{N_u} A_n \int_y^R \frac{\varepsilon_n(r)}{\sqrt{r^2 - y^2}} rdr \tag{8}$$

where $i(y)$ denotes a lateral intensity fitted by a set of cosine-functions.

The integrals

$$I_n(y) = \int_y^R \frac{\varepsilon_n(r)}{\sqrt{r^2 - y^2}} rdr \tag{9}$$

cannot be solved analytically but calculated numerically. The amplitudes A_n are still unknown, but applying Eq. (8) to be the least squares fitted to the measured data $I(y)$ at each measurement position y_k, one obtains:

$$\sum_{k=1}^{K}\left(i(y_k) - I(y_k)^2\right) \rightarrow Min. \tag{10}$$

The insertion of Eq. (8) into Eq. (10) followed by analytical differentiation with respect to the unknown amplitudes A_n leads to

$$2\sum_{n=N_l}^{N_u}\left(A_n \sum_{k=1}^{K}(I_n(y_k)I_m(y_k))\right) = \sum_{k=1}^{K}(I(y_k)I_m(y_k))(\forall m : N_l \leq m \leq N_u). \tag{11}$$

Evaluation of Eq. (11) yields the amplitudes A_n, which are inserted into Eq. (6) producing the deconvoluted $\varepsilon(r)$.

The Abel inversion process was done by Matlab R2016a. The implementation of Abel inversion in Matlab was directly downloaded from the website of MathWorks, which was shared by C. Killer [34]. In this Matlab code, a deconvoluted profile $\varepsilon(r)$ can be obtained by an input of the measured data points $I(y_k)$, radius R of the plasma jet and an upper-frequency limit N_u. Following this method, the numerical inversion can be used as a noise filter by choosing the lower and upper frequency limits N_l and N_u in Eq. (11). In the Matlab code, N_l was set to 1, so N_u defines the number of cosine expansions. Choosing a high value of N_u would give more potential features of measured intensity while a low value of N_u results in a low-pass filtering effect, reducing the noise. Therefore, the value of N_u was

set to 10 to achieve an efficient low-pass filtering because the deconvolution is almost entirely determined by the low-frequency components.

Results and Discussion

Local Emission Intensity Profiles

In order to compare the intensities at different chamber pressures, the intensities are normalized. Examples of measured raw data and polynomial fits of Ar I and Ar II (singly ionized argon) lines under conditions A-200 (Ar/He jet, 200 Pa) and A-1000 (Ar/He jet, 1000 Pa) are given in Fig. 3. Under the same conditions, all the measured intensity profiles of Ar lines at different wavelengths have the similar shape as in Fig. 3. It can be seen that the highest measured intensity of the Ar I line at a chamber pressure of 200 Pa is achieved at approx. $y = 40$ mm while that of the Ar II line is near the center of the plasma jet, which means that Ar is ionized in the center of the plasma jet. Since the measured intensity $I(y)$ corresponds to the integration along the line of measurement, one can speculate that in the center of plasma jet the concentration of neutral Ar must be low. As drawn in Fig. 3, a dashed line describing the 5% level of the normalized value is plotted to give a more reliable description of the radial jet extensions where the values approach zero.

Figure 4 gives the reconstructed $\varepsilon(r)$ from the measured $I(y)$ (shown in Fig. 3) with $N_u = 10$. At a chamber pressure of 200 Pa, in the center of the plasma jet ($r = 0$ mm), the $\varepsilon(r)$ of Ar I results slightly negative. It should be noted that with increasing N_u, this feature of negative $\varepsilon(r)$ does not change. A reconstruction from the obtained $\varepsilon(r)$ to $I'(y)$ (by
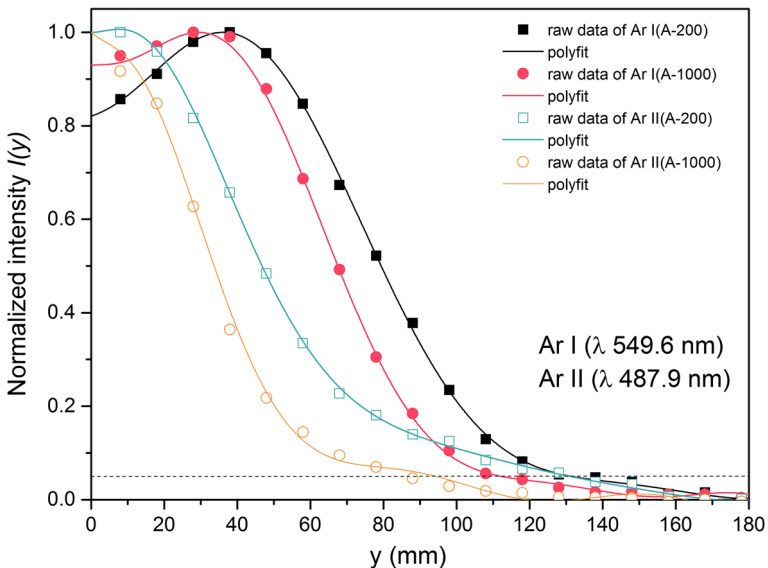

Fig. 3 Radial profiles of measured $I(y)$ (normalized) of Ar I line (549.6 nm) and Ar II line (487.9 nm) under conditions A-200 (Ar/He jet, 200 Pa) and A-1000 (Ar/He jet, 1000 Pa); The raw data points are the experimentally measured $I(y)$ and the *lines* are polynomial fits of the raw data; The *dashed line* describes the 5% level of the normalized $I(y)$
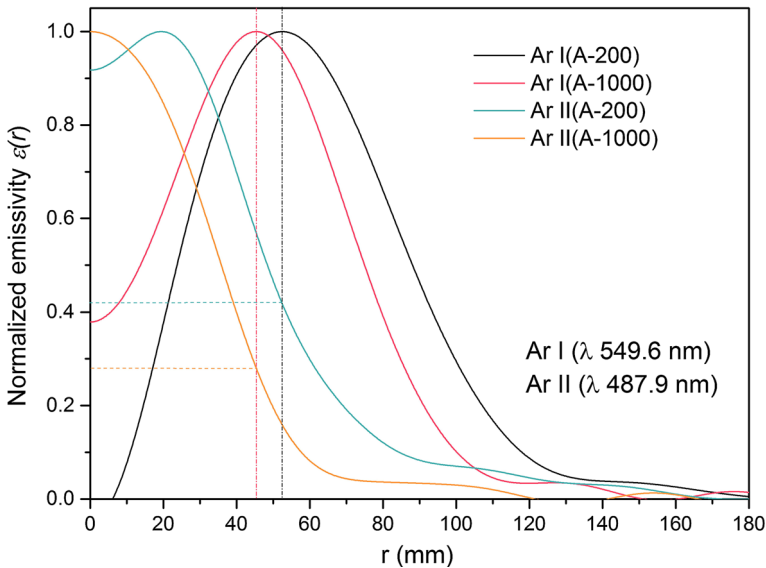
Fig. 4 Radial profile of the reconstructed $\varepsilon(r)$ of Ar I line (549.6 nm) and Ar II line (487.9 nm) under conditions A-200 (Ar/He jet, 200 Pa) and A-1000 (Ar/He jet, 1000 Pa); The *dashed lines* describe the radii where the $\varepsilon(r)$ of Ar I line reaches the maximum value and the corresponding $\varepsilon(r)$ of Ar II line

numerical integration $I'(y) = \int_{-x_0}^{x_0} \varepsilon(r)dx$ with $x = \sqrt{r^2 - y^2}$) confirmed that $I'(y)$ has only average deviations of 5% from the measured $I(y)$. Note that the emission intensity is positively proportional to the concentration of the species and exponential to the temperature. Such low values of $\varepsilon(r = 0\,mm)$ in the center of plasma jet might be caused, on one hand, by the low concentration of neutral Ar due to the ionization of Ar. On the other hand, the measurement error could also lead to slightly negative values in the center [35]. When the chamber pressure increased to 1000 Pa, the relative $\varepsilon(r = 0\,mm)$ is much higher which could be due to the relatively enhancive concentration of neutral Ar. As indicated in Ref. [36], when increasing the radius in a pure argon plasma, the $\varepsilon(r)$ of the ionic line is expected to reach its minimum value at the approximate radius where the emission of the atomic line has its maximum. However, as shown in Fig. 4, at chamber pressure 200 Pa, the Ar II line still has around 42% relative intensity, which means that the addition of He to argon plasma seems to have an influence on the distribution of ionic and neutral Ar in the center of the plasma jet.

When hydrogen was added to the plasma gases at the pressure of 200 Pa, the measured intensities of all lines were much lower than that in the Ar/He jet. In Fig. 5, it can be seen that both the measured intensities $I(y)$ and the emissivities $\varepsilon(r)$ of the Ar I line at 549.6 nm approach zero at a radius of approx. 90 mm. Although the $\varepsilon(r = 0\,mm)$ of the Ar I line has a lower value, its relative value is not as low as under condition A-200 (Fig. 4). The possible reasons are lower plasma jet temperatures and thus lower ionization degrees of argon under this condition.

However, as shown in Fig. 6, both the measured intensities $I(y)$ and the emissivities $\varepsilon(r)$ of the hydrogen line (H$_\beta$ 486.1 nm) drop to 5% level of the maximum $I(y)$ at a rather large
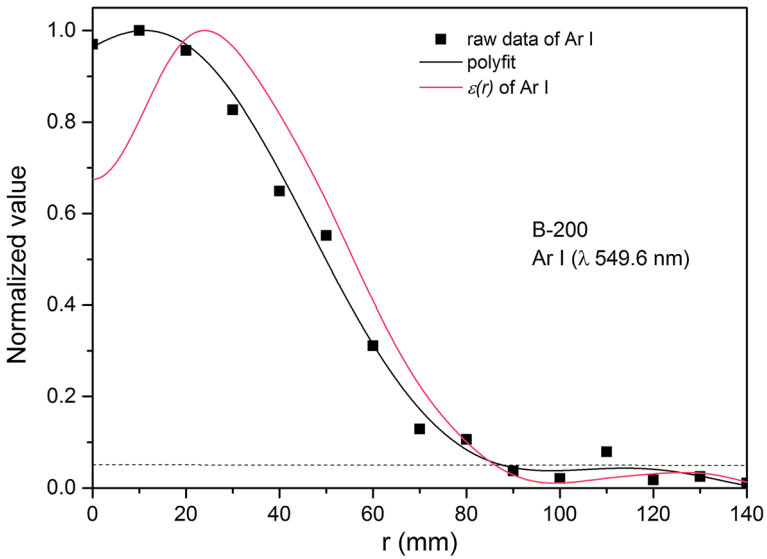
Fig. 5 Radial profile of measured *I(y)*, polynomial fits of raw data and the reconstructed *ε(r)* of Ar I line (549.6 nm) under condition B-200 (Ar/He/H₂ jet, 200 Pa); The *dashed line* describes the 5% level of the normalized value

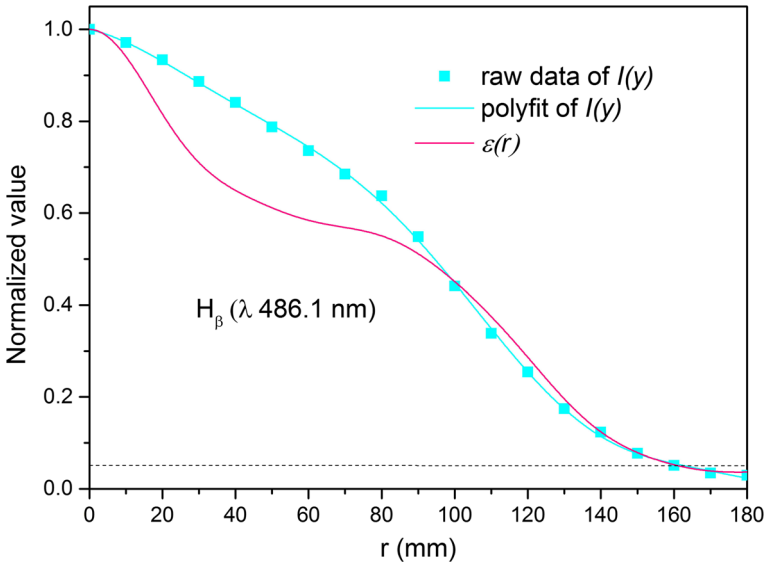**Fig. 6** Radial profile of measured *I(y)*, polynomial fits of raw data and the reconstructed *ε(r)* of H$_\beta$ line (486.1 nm) under condition B-200 (Ar/He/H₂ jet, 200 Pa); The *dashed line* describes the 5% level of the normalized value

radius of approx. 160 mm, which is obviously the reason for the broader plasma jet appearance under condition B-200 (Ar/He/H₂ jet, 200 Pa) compared to condition A-200 (Ar/He jet, 200 Pa) (the photos of the plasma jets can be found in the Fig. 1 of Ref. [18]).

Temperatures

Excitation Temperature Profiles

Since the reconstructed $\varepsilon(r)$ profiles of Ar I lines drop to 5% level of the maximum value at $r = 130$, 110 and 90 mm under conditions A-200, A-1000 and B-200, respectively, The errors in the temperature calculations beyond the radii become quite large. Therefore, the T_{exc} profiles were calculated only up to these radii. By replacing an $I(y)$ with a $\varepsilon(r)$ and eliminating the L in Eq. (2), the local excitation temperature $T_{exc}(r)$ can be obtained from the slope of a linear Boltzmann plot. Under condition A-200, due to the very low emission of Ar I lines in the center of plasma (seen in Fig. 4), it is not possible to apply the Boltzmann plot method to calculate the local excitation temperature $T_{exc}(r)$ anymore because of the large uncertainty. But beyond a radius of 15 mm, the enhancive emissivities indicate the increasing amount of neutral argon. Therefore, the $T_{exc}(r)$ profiles of argon under condition A-200 were calculated starting from $r = 15$ mm.

Under condition A-200, $T_{exc}(r = 15$ mm$)$ is about 7000 K and $T_{exc}(r > 15$ mm$)$ decreases along the radial direction as given in Fig. 7a. When the chamber pressure increases to 1000 Pa, the calculated temperature $T_{exc}(r)$ for A-1000 is much lower than that at 200 Pa. The $T_{exc}(r)$ for A-1000 decreased by 250 K from $r = 0$ mm to $r = 40$ mm and then slightly increased along the radial direction. This apparently increasing temperature at the outer fringe of the plasma jet is unreasonable. A straight line may be obtained in the Boltzmann plot even when non-LTE levels are included, thus leading to a spurious excitation temperatures [28]. In the case of a recombining plasma, the underpopulation of low energy levels leads to a higher excitation temperature. In other words, at the periphery of the plasma jet, all chosen levels might be not in LTE so that the obtained T_{exc} becomes spuriously high. The same phenomenon can be also found when the temperature was calculated with neutral helium (He I) lines. Seven He I lines were chosen as in Ref. [14] to calculate the excitation temperature. As shown in Fig. 7b, the calculated excitation temperature of He dropped slightly and then increased dramatically along the radial direction until reaching the outer fringe where it stopped to increase. The possible reason could be that, in the outer fringe region, the density of electrons is not sufficient to sustain LTE, in particular for He typically exhibiting a strong deviation from LTE as mentioned before.

Therefore, under condition B-200 (Ar/He/H$_2$ jet, 200 Pa), the temperature was also calculated by Ar I lines as under condition A. In Fig. 7a, it is obvious that the Ar/He/H$_2$ jet has lower $T_{exc}(r)$ compared with Ar/He jet only similar at radii of 40 and 50 mm. And the $T_{exc}(r)$ starts to drop very fast at $r > 50$ mm down to $T_{exc}(r = 90$ mm$) = 2500$ K.

Substrate Temperatures

As the substrate temperature (T_s) has a major influence on the microstructure of the coatings made by thin film deposition [37], T_s was recorded continuously by pyrometer at different stages through the whole coating process at a spraying distance of 1000 mm. The results are given in Fig. 8. In the first stage of the experiment, the current was adjusted approaching to the appropriate current step by step so that T_s kept increasing. After the currents became stable, T_s reached a maximum value and then kept rather constant. In the third stage, the carrier gas was changed from 2×8 slpm to 2×16 slpm, which led to a slight T_s drop under both conditions. One reason could be that adding of carrier gas reduced the plasma jet temperature and thus the substrate temperature decreased. Later,
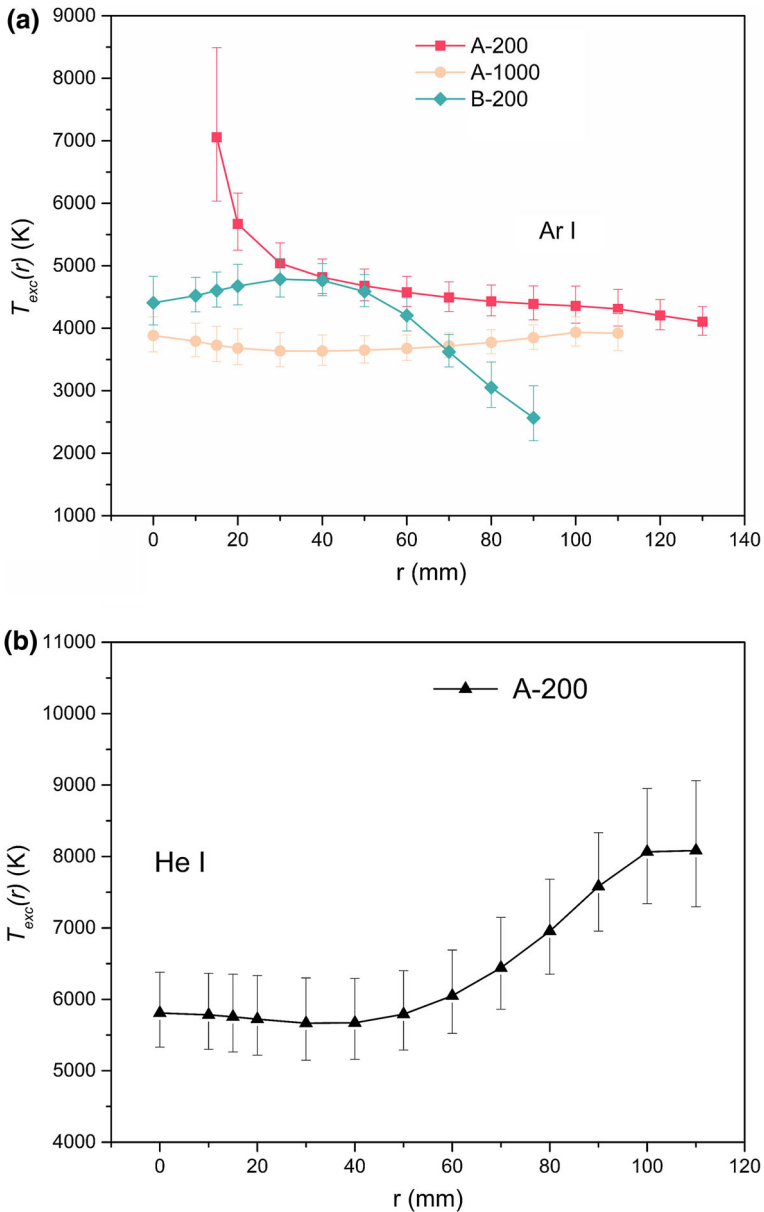
Fig. 7 **a** Development of the excitation temperatures along the radial direction of the plasma jets under condition A-200 (Ar/He jet, 200 Pa), A-1000 (Ar/He jet, 1000 Pa) and B-200 (Ar/He/H$_2$ jet, 200 Pa); **b** calculated temperatures by He I lines along the radial direction of the plasma jet under condition A-200 (Ar/He jet, 200 Pa)

after T_s was stable again, O$_2$ (4 slpm) was let into the chamber which did not cause any apparent temperature variation. After feeding powder into the chamber, the temperatures decreased gradually. One reason is that the powder absorbed energy from the plasma (loading effect of powder will be discussed later). The other reason is assumed to be the
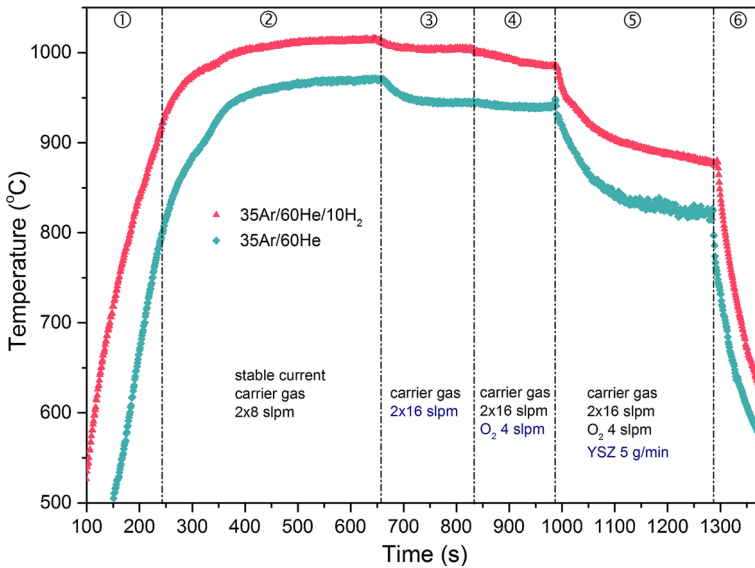
Fig. 8 Substrate temperatures under conditions A-200 (Ar/He jet, 200 Pa, *green curve*) and B-200 (Ar/He/H$_2$ jet, 200 Pa, *red curve*) measured at 1000 mm spraying distance

emissivity change of the target surface due to the coating formation. As the coating grows, the surface becomes rougher while the internal porosity increases.

On one hand, the overall T_s under condition B-200 (Ar/He/H$_2$ jet, 200 Pa) was about 50 K higher than that under condition A-200 (Ar/He jet, 200 Pa). On the other hand, the T_{exc} of Ar/He jet at 200 Pa was higher as shown in Fig. 7a. The reason for this abnormal phenomenon could be caused by the enhanced reaction thermal conductivity of H$_2$ in the temperature range of 2000 K to 5000 K due to the dissociation of H$_2$ as presented in Ref. [38]. Thus, the specific heat capacity (c$_p$) and thermal conductivity under chemical equilibrium were calculated with the CEA software assigning discrete temperatures and the chamber pressure [39, 40]. As shown in Fig. 9a, the peak of c$_p$ in the temperature range of 2000–3000 K in the Ar/He/H$_2$ jet is due to the dissociation of H$_2$. The dissociation energy is consumed without contributing to an increase of the temperature. And this could be one reason that the Ar/He/H$_2$ jet has a relatively low excitation temperature compared to the Ar/He jet. Similarly, the dissociation of H$_2$ increases the reaction thermal conductivity (Fig. 9b) of the Ar/He/H$_2$ jet. In comparison, in the range of calculated $T_{exc}(r)$, the thermal conductivity of Ar/He/H$_2$ jet is distinctly higher than that of Ar/He jet, especially around 2500 K. This could be the reason why under condition B-200, $T_{exc}(r)$ is relatively low but T_s is higher compared to condition A-200.

Concentration Profiles of Ar and He

Considering that He is prone to serious deviations from LTE at the fringe region of the PS-PVD plasma jet, the calculation of concentration profiles becomes quite complicate. In this section, a rough but simple method is discussed to estimate the constituent concentration profiles in the Ar/He plasma jet.
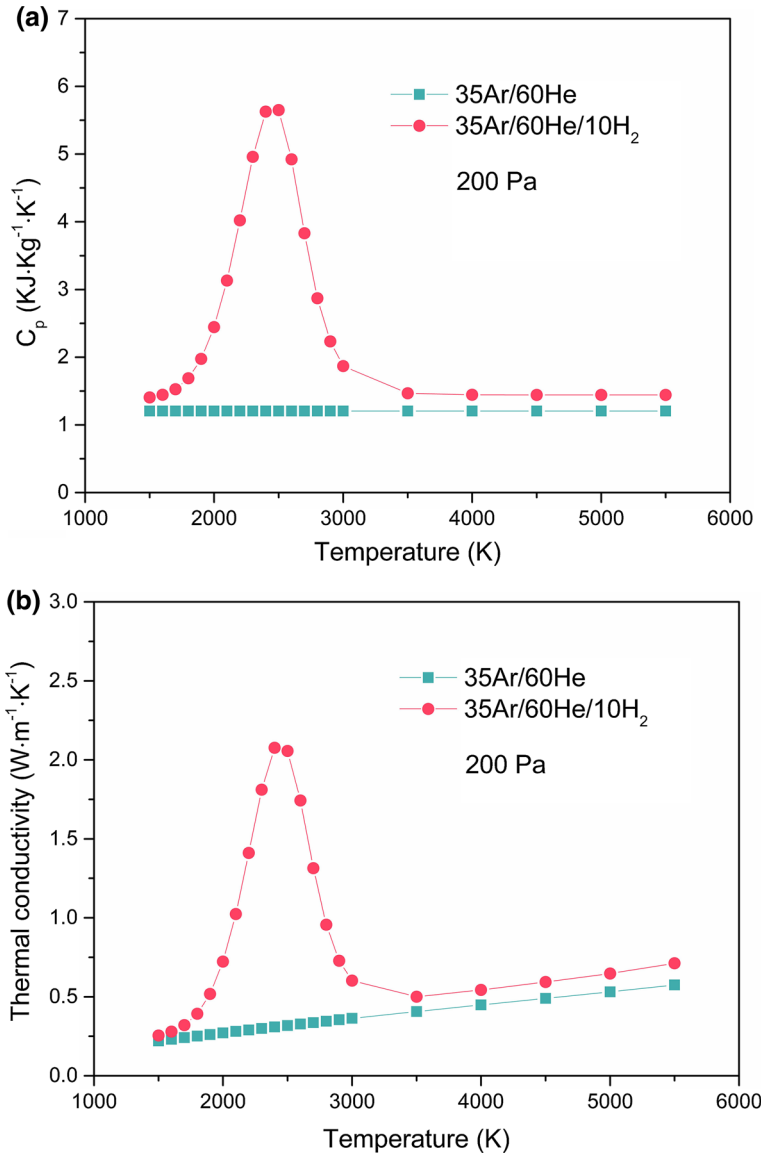
Fig. 9 Calculated **a** specific heat capacity (c_p) and **b** thermal conductivity profiles under conditions A-200 (Ar/He jet, 200 Pa) and B-200 (Ar/He/H_2 jet, 200 Pa)

Assuming LTE condition in PS-PVD, the excited states can still be illustrated by Boltzmann distribution. As the intercept of Eq. (2), $C = ln\left(\frac{Lhcn_{tot}(r)}{4\pi Z}\right)$, is related to n_{tot}, the ratio between atomic Ar and atomic He in the plasma can be calculated according to Eq. (12) at every given radius:

$$\frac{n_{tot}(Ar)}{n_{tot}(He)} = \frac{exp(C(Ar))Z(Ar)}{exp(C(He))Z(He)} \tag{12}$$

wherein, $C(Ar)$ and $C(He)$ can be obtained from the intercept of the Boltzmann plots. The values of the partition functions $Z(Ar)$ and $Z(He)$ are retrieved from NIST Atomic Spectra Database [23], in which the element and its ionization stage have to be specified as well as the temperature for determining the partition function. In the case of Ar I and He I, both of $Z(Ar)$ and $Z(He)$ are almost equal to unity in the temperature range of 0.1 eV (1160.5 K)–1 eV (11,605 K), therefore Eq. (12) can be simplified as:

$$\frac{n_{tot}(Ar)}{n_{tot}(He)} = \frac{exp(C(Ar))}{exp(C(He))} \tag{13}$$

Using this approach, the $n_{tot}(Ar)/n_{tot}(He)$ ratio can be determined along the radial direction. As seen in Fig. 10, the increasing $n_{tot}(Ar)/n_{tot}(He)$ ratio with increasing r indicates that in the center of plasma jet the main constitute is atomic He while atomic Ar prevails mainly at the periphery of helium flow. However, it should be noted that the under-population of low energy levels leads to higher spurious excitation temperatures as well as to smaller values of C, especially for He. Thus, the calculated results in Fig. 10 could be higher than the real value of $n_{tot}(Ar)/n_{tot}(He)$ especially at the outer fringe region where $T_{exc}(r)$ of He shows spurious high values as mentioned in Fig. 7b. But the increasing tendency of $n_{tot}(Ar)/n_{tot}(He)$ should be correct. The input ratio of Ar and He is $35/60 \approx 0.58$ as indicated by the dashed line in Fig. 10. When the chamber pressure increased from 200 Pa to 1000 Pa, the plasma jet becomes shorter and narrower. Hence, the calculated $n_{tot}(Ar)/n_{tot}(He)$ values reached this input ratio at a smaller radius. The uncertainty of the ratio of concentration in Fig. 10 is estimated by calculating the ratios in Eq. (13) with the standard errors of $C(Ar)$ and $C(He)$ of the linear fit. Here, it is assumed
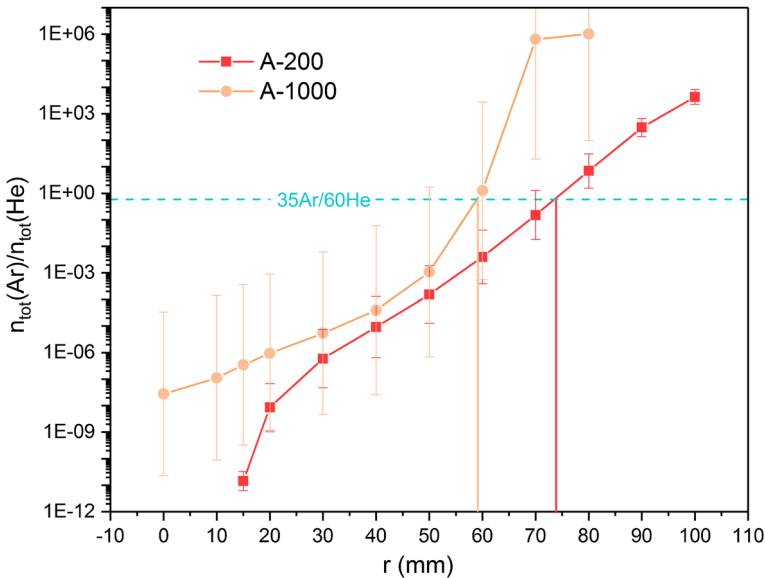

Fig. 10 Ratio of concentration between atomic Ar and atomic He under conditions A-200 (Ar/He jet, 200 Pa) and A-1000 (Ar/He jet, 1000 Pa)

that the absence of LTE affects the fitting quality. The uncertainty actually increases from the center region to the outer fringe region of the plasma jet. Because the values in Fig. 10 are given in "log" format, the increasing tendency is not very evident in the diagram. Besides, one can see that the uncertainties of the ratios under condition A-1000 are larger than those under condition A-200. This could be another indication of severe absence from LTE under condition A-1000.

Besides, as mentioned in "Intensity and Emissivity Profiles" section, in the center of plasma jet, Ar is mainly ionized so that the $\varepsilon(r)$ of atomic Ar is low. However, the ionization of Ar is obviously not the only reason for the low $\varepsilon(r)$ of neutral Ar, as the demixing of Ar and He can be another reason. The demixing of Ar and He in atmospheric-pressure free-burning arcs has been investigated by A. B. Murphy, who found that demixing almost always has a large influence on arc composition and helium concentration in the center of an argon-helium arc [41]. In an argon-helium arc, the three categorical demixing processes (mole fraction (partial pressure gradient), frictional force, thermal diffusion) can contribute to the increase of the helium mass fraction in the regions at higher temperatures. Under PS-PVD conditions, the plasma is very thin and therefore the influence of frictional forces caused by collisional interactions might be small. However, in the center region of the plasma jet, Ar is ionized but He is not ionized due to its high ionization energy. This will cause a mole fraction gradient leading to an increase in the mass fraction of He in the high-temperature region. Besides, according to the $T_{exc}(r)$ of Ar (Fig. 7a in "Intensity and Emissivity Profiles" section), a temperature gradient is present along the radial direction of the plasma jet, which further concentrates helium in the higher-temperature region. Thus, the mole fraction gradients caused by ionization of Ar as well as by thermal diffusion could lead to an increase of non-ionized and light He in the center (high-temperature) region of the plasma jet.

Effect of Powder Loading

Although a more accurate excitation temperature can be obtained by Abel inversion transforming measured $I(y)$ into $\varepsilon(r)$, the laborious data processing of Abel inversion complicates the application of OES. Hence, the measured integral $I(y)$ without Abel inversion are more favored to estimate the average excitation temperature $T_{exc}^{(A)}$ of a plasma jet in engineering applications. In particular, with the injection of powder, the vapor species from evaporated feedstock power has an influence on general plasma properties such as a cooling effect [42]. Therefore, with the injection of feedstock into the plasma, $T_{exc}^{(A)}$ of Ar at different powder feeding rates were calculated based on the measured $I(y = 0 \text{ mm})$ by applying Boltzmann plot method without Abel inversion. An alternative method proposed in Ref. [43] to calculate axial plasma temperatures without Abel inversion was also employed. However, the results show that the axial temperature was approx. 100 K higher than the corresponding $T_{exc}^{(A)}$, but lower than the $T_{exc}(0)$ obtained by Abel inversion. The possible reason might be that the LTE is not satisfied. Thus, the uncorrected $T_{exc}^{(A)}$ were considered to be representative of an average jet temperature.

As shown in Fig. 11, under condition A-200, when the powder was injected with a small rate of 3.8 g/min into the plasma jet, the powder loading effect was found as the $T_{exc}^{(A)}$ reduced by 360 K. With increasing powder feeding rates, $T_{exc}^{(A)}$ decreases degressively and approaches 4000 K. The same powder loading effect can be found under condition B-200 as well. In this case, only one powder feed rate 6.9 g/min was tested, which led to about 320 K drop of the $T_{exc}^{(A)}$ smaller than 500 K in the case of condition A-200.
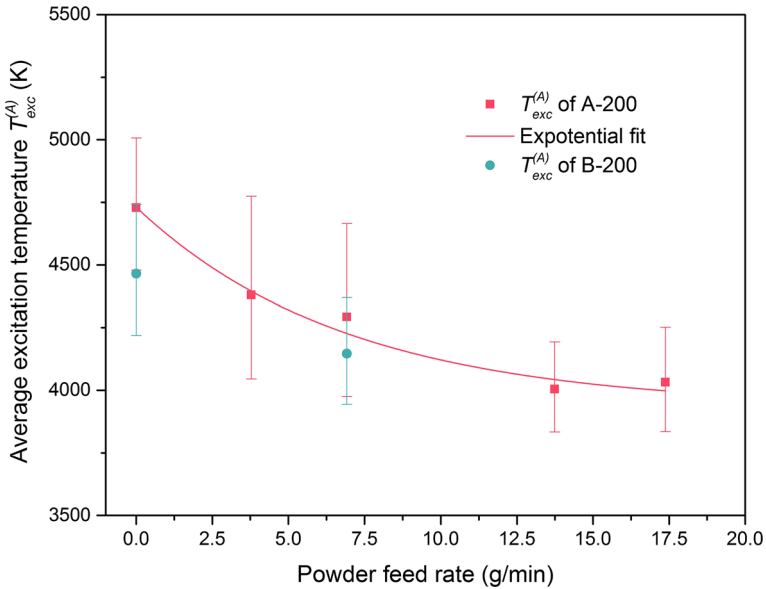
Fig. 11 Variation of average excitation temperatures $T_{exc}^{(A)}$ determined for different powder feeding rates under conditions A-200 (Ar/He jet, 200 Pa) and B-200 (Ar/He/H$_2$ jet, 200 Pa)

Conclusions

In this paper, the characteristics of Ar/He and Ar/He/H$_2$ plasma jet under PS-PVD conditions were investigated by OES. The main conclusions are as following:

- Abel inversion was introduced to obtain the local distribution of emission intensity. Thus, it became possible to determine the development of the excitation temperatures calculated by the Boltzmann plot method along the radial direction of the plasma jet. From the center to the edge of the plasma jet, the local excitation temperature $T_{exc}(r)$ of Ar decreases gradually. Helium was found to deviate from LTE even where argon is still in LTE, which leads to apparently higher excitation temperatures at the fringe of the plasma jet.
- A robust and simple method was proposed to estimate concentration profiles of atomic Ar/He in the plasma jet. In the central region, the ionization of Ar is one of the reasons for the very low ratio between atomic argon and helium concentrations $n_{tot}(Ar)/n_{tot}(He)$; other reasons could be demixing effects.
- The addition of hydrogen into the plasma gas reduces the excitation temperature in the plasma jet but leading to a relatively high substrate temperature due to the high thermal conductivity induced by the dissociation of hydrogen in the temperature range of 2000 K to 3000 K.
- The injections of feedstock powder into the plasma jet results in a decrease of the jet temperature, however the overall average jet temperatures still remained above 4000 K.

References

1. Mauer G, Hospach A, Vaßen R (2013) Process conditions and microstructures of ceramic coatings by gas phase deposition based on plasma spraying. Surf Coat Technol 220:219–224
2. Kim HJ, Hong SH (1995) Comparative measurements on thermal plasma jet characteristics in atmospheric and low pressure plasma sprayings. IEEE Trans Plasma Sci 23(5):852–859
3. Mauer G, Vaßen R, Stöver D (2011) Plasma and particle temperature measurements in thermal spray: approaches and applications. J Therm Spray Technol 20(3):391–406
4. Buchner P, Schubert H, Uhlenbusch J, Willée K (1999) Modeling and spectroscopic investigations on the evaporation of zirconia in a thermal rf plasma. Plasma Chem Plasma Process 19(3):341–362
5. Green KM, Borras MC, Woskov PP, Flores GJ III, Hadidi K, Thomas P (2001) Electronic excitation temperature profiles in an air microwave plasma torch. IEEE Trans Plasma Sci 29(2):399–406
6. Semenov S, Cetegen B (2001) Spectroscopic temperature measurements in direct current arc plasma jets used in thermal spray processing of materials. J Therm Spray Technol 10(2):326–336
7. Yotsombat B, Davydov S, Poolcharaunsin P, Vilaithong T, Brown IG (2001) Optical emission spectra of a copper plasma produced by a metal vapour vacuum arc plasma source. J Phys D Appl Phys 34(12):1928–1932
8. Jankowski K, Jackowska A (2007) Spectroscopic diagnostics for evaluation of the analytical potential of argon+helium microwave-induced plasma with solution nebulization. J Anal At Spectrom 22(9):1076–1082
9. Refke A, Gindrat M, AG SM (2007) Process characterization of LPPS thin film processes with optical diagnostics. In: Marple BR, Hyland MM, Lau Y -C, Li C -J, Lima RS, Montavon G (eds) Thermal spray 2007: global coating solutions. ASM International, Material Park, pp 826–831
10. Mauer G, Vaßen R, Stöver D (2010) Thin and dense ceramic coatings by plasma spraying at very low pressure. J Therm Spray Technol 19(1–2):495–501
11. Hospach A, Mauer G, Vaßen R, Stöver D (2011) Columnar-structured thermal barrier coatings (TBCs) by thin film low-pressure plasma spraying (LPPS-TF). J Therm Spray Technol 20(1–2):116–120
12. Zotov N, Hospach A, Mauer G, Sebold D, Vaßen R (2011) Deposition of La–Sr–Fe–Co perovskite coatings with different microstructures by low pressure plasma spraying. J Therm Spray Technol 21(3–4):7
13. Hospach A, Mauer G, Vaßen R, Stöver D (2012) Characteristics of ceramic coatings made by thin film low pressure plasma spraying (LPPS-TF). J Therm Spray Technol 21(3–4):435–440
14. Mauer G, Vaßen R (2012) Plasma spray-PVD: plasma characteristics and impact on coating properties. J Phys Conf Ser 406:012005
15. Mauer G (2014) Plasma characteristics and plasma-feedstock interaction under PS-PVD process conditions. Plasma Chem Plasma Process 34(5):1171–1186
16. Rezanka S, Mauer G, Vaßen R (2014) Improved thermal cycling durability of thermal barrier coatings manufactured by PS-PVD. J Therm Spray Technol 23(1–2):182–189
17. Chen Q-Y, Peng X-Z, Yang G-J, Li C-X, Li C-J (2015) Characterization of plasma jet in plasma spray-physical vapor deposition of YSZ using a <80 kW shrouded torch based on optical emission spectroscopy. J Therm Spray Technol 24(6):1038–1045
18. Mauer G, Hospach A, Zotov N, Vaßen R (2013) Process development and coating characteristics of plasma spray-PVD. J Therm Spray Technol 22(2–3):83–89
19. He W, Mauer G, Gindrat M, Wäger R, Vaßen R (2016) Investigations on the nature of ceramic deposits in plasma spray-physical vapor deposition. J Therm Spray Technol 26(1–2):83–92
20. Shanmugavelayutham G, Selvarajan V, Padmanabhan PVA, Sreekumar KP, Joshi NK (2007) Effect of powder loading on the excitation temperature of a plasma jet in DC thermal plasma spray torch. Curr Appl Phys 7(2):186–192
21. Bockasten K (1961) Transformation of observed radiances into radial distribution of the emission of a plasma. J Opt Soc Am 51(9):943–947
22. Mauer G, Marqués-López J-L, Vaßen R, Stöver D (2007) Detection of wear in one-cathode plasma torch electrodes and its impact on velocity and temperature of injected particles. J Therm Spray Technol 16(5–6):933–939
23. NIST Atomic Spectra Database (ver. 5.3) (2015). http://physics.nist.gov/asd. Accessed 30 Nov 2015

24. Calzada M, Moisan M, Gamero A, Sola A (1996) Experimental investigation and characterization of the departure from local thermodynamic equilibrium along a surface-wave-sustained discharge at atmospheric pressure. J Appl Phys 80(1):46–55
25. van der Mullen JAM (1990) Excitation equilibria in plasmas; a classification. Phys Rep 191(2):109–220
26. Mitchner M, Kruger CH (1973) Partially ionized gases. Wiley, New York
27. Rat V, Murphy A, Aubreton J, Elchinger M-F, Fauchais P (2008) Treatment of non-equilibrium phenomena in thermal plasma flows. J Phys D Appl Phys 41(18):183001
28. Quintero M, Rodero A, Garcia M, Sola A (1997) Determination of the excitation temperature in a nonthermodynamic-equilibrium high-pressure helium microwave plasma torch. Appl Spectrosc 51(6):778–784
29. Jonkers J, Van der Mullen J (1999) The excitation temperature in (helium) plasmas. J Quant Spectrosc Radiat Transfer 61(5):703–709
30. Abel NH (1826) Auflösung einer mechanischen Aufgabe. Journal für die reine und angewandte Mathematik 1:5 **(in German)**
31. Chan GC-Y, Hieftje GM (2006) Estimation of confidence intervals for radial emissivity and optimization of data treatment techniques in Abel inversion. Spectrochim Acta Part B At Spectrosc 61(1):31–41
32. Pretzler G (1991) A new method for numerical Abel-inversion. Z Naturforsch A Phys Sci 46(7):639–641
33. Pretzler G, Jäger H, Neger T, Philipp H, Woisetschläger J (1992) Comparison of different methods of abel inversion using computer simulated and experimental side-on data. Z Naturforsch A Phys Sci 47(9):955–970
34. Abel Inversion Algorithm (2013) © 1994–2017 The MathWorks, Inc. https://cn.mathworks.com/matlabcentral/fileexchange/43639-abel-inversion-algorithm. Accessed 20 Mar 2016
35. Ramsey A, Diesso M (1999) Abel inversions: error propagation and inversion reliability. Rev Sci Instrum 70(1):380–383
36. Olsen H (1959) Thermal and electrical properties of an argon plasma. Phys Fluids (1958–1988) 2(6):614–623
37. Thornton JA (1986) The microstructure of sputter-deposited coatings. J Vac Sci Technol A 4(6):3059–3065
38. Murphy A (2000) Transport coefficients of hydrogen and argon–hydrogen plasmas. Plasma Chem Plasma Process 20(3):279–297
39. Gordon S, McBride BJ (1996) Computer program for calculation of complex chemical equilibrium compositions and applications—user's manual and program description, part 2. NASA-Reference Publication 1311
40. Gordon S, McBride BJ (1994) Computer program for calculation of complex chemical equilibrium compositions and applications—analysis, part 1. NASA-Reference Publication, 1311
41. Murphy A (1997) Demixing in free-burning arcs. Phys Rev E 55(6):7473
42. Gleizes A, Cressault Y (2017) Effect of metal vapours on the radiation properties of thermal plasmas. Plasma Chem Plasma Process 37(3):20
43. Marotta A (1994) Determination of axial thermal plasma temperatures without Abel inversion. J Phys D Appl Phys 27(2):268